Articles

DNA Cleavage by *Eco*RV Endonuclease: Two Metal Ions in Three Metal Ion Binding Sites†

Nancy C. Horton‡ and John J. Perona*

Department of Chemistry and Biochemistry and Interdepartmental Program in Biomolecular Science and Engineering, University of California at Santa Barbara, Santa Barbara, California 93106-9510

Received January 12, 2004; Revised Manuscript Received April 1, 2004

ABSTRACT: Four crystal structures of *Eco*RV endonuclease mutants K92A and K38A provide new insight into the mechanism of DNA bending and the structural basis for metal-dependent phosphodiester bond cleavage. The removal of a key active site positive charge in the uncleaved K92A−DNA−M^{2+} substrate complex results in binding of a sodium ion in the position of the amine nitrogen, suggesting a key role for a positive charge at this position in stabilizing the sharp DNA bend prior to cleavage. By contrast, two structures of K38A cocrystallized with DNA and Mn^{2+} ions in different lattice environments reveal cleaved product complexes featuring a common, novel conformation of the scissile phosphate group as compared to all previous *Eco*RV structures. In these structures, the released 5′-phosphate and 3′-OH groups remain in close juxtaposition with each other and with two Mn^{2+} ions that bridge the conserved active site carboxylates. The scissile phosphates are found midway between their positions in the prereactive substrate and postreactive product complexes of the wild-type enzyme. Mn^{2+} ions occupy two of the three sites previously described in the prereactive complexes and are plausibly positioned to generate the nucleophilic hydroxide ion, to compensate for the incipient additional negative charge in the transition state, and to ionize a second water for protonation of the 3′-oxyanion. Reconciliation of these findings with earlier X-ray and fluorescence studies suggests a novel mechanism in which a single initially bound metal ion in a third distinct site undergoes a shift in position together with movement of the scissile phosphate deeper into the active site cleft. This reconfigures the local environment to permit binding of the second metal ion followed by movement toward the pentacovalent transition state. The new mechanism suggested here embodies key features of previously proposed two- and three-metal catalytic models, and offers a view of the stereochemical pathway that integrates much of the copious structural and functional data that are available from exhaustive studies in many laboratories.

Many enzymes that cleave duplex DNA require divalent metal ions for their catalytic function, including topoisomerases, site-specific recombinases and transposases, nucleases involved in DNA repair processes, and bacterial restriction endonucleases (*1*−*8*). A paradigm for how metal ions promote the chemically difficult hydrolysis of DNA has emerged from studies of the 3′−5′ exonuclease activity of *Escherichia coli* DNA polymerase I (*9*, *10*). In this mechanism, two metal ions are positioned parallel to the apical axis of the trigonal bipyramidal transition state, where they interact with both the attacking nucleophile and the leaving group. One metal ion activates the nucleophilic water molecule by lowering its pK_a, thus facilitating generation of the attacking hydroxide ion. The second metal directly ligates the leaving oxygen, facilitating bond breakage by neutralizing its developing negative charge. Both metals also ligate a nonbridging oxygen of the scissile phosphate to aid in substrate positioning and to compensate for the incipient additional negative charge in the transition state.

Restriction endonucleases are important model systems for the further exploration of metal-dependent phosphoryl transfer, as well as the coupling of DNA cleavage with exquisite sequence selectivity (*11*). To date, most work has been done on the orthodox type II enzymes, which are homodimeric proteins that recognize palindromic DNA sequences 4−8 bp in length. While the X-ray structures of six restriction enzymes in this class have been determined bound in ternary complexes with specific DNA and divalent metal ions, only *Eco*RV has been studied extensively from both enzymological and crystallographic perspectives. *Eco*RV cleaves its dyad-symmetric GATATC target site in a blunt-ended fashion at the center TA step (*12*). The two product duplexes possess 5′-phosphate and 3′-OH groups, as found for all type II restriction enzymes. Single-base substitutions within the

† Supported by NIH Grant GM53763 (to J.J.P.) and by American Cancer Society Postdoctoral Fellowship PF-98-015-GMC (to N.C.H.) and an NSF-POWRE award (to N.C.H.).

* To whom correspondence should be addressed. Telephone: (805) 893-7389. Fax: (805) 893-4120. E-mail: perona@chem.ucsb.edu.

‡ Current address: Department of Biochemistry and Molecular Biophysics, University of Arizona, Tucson, AZ 85721.

10.1021/bi0499056 CCC: $27.50
Published on Web 05/12/2004

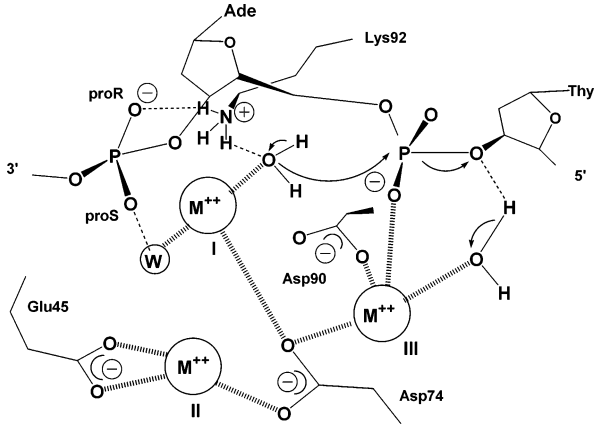

FIGURE 1: Three-metal mechanism for the transition state of DNA cleavage by *Eco*RV (*24*, *29*). The metal ion located in site I generates the attacking hydroxide nucleophile, which is stabilized and oriented by the positively charged Lys92. The site III metal stabilizes the incipient additional negative charge in the transition state and aids in water-mediated protonation of the leaving group. The site II metal plays a structural role. An analogous mechanism in which Lys92 is unprotonated and functions as a general base has also been proposed (*29*).

cognate site result in decreases in k_{cat}/K_m of 10^6-fold, highlighting the very strong sequence specificity (*13*).

All steps along the *Eco*RV reaction pathway depend on the presence of divalent metals. The affinity of DNA for the cognate target sequence is increased by roughly 10^4-fold by metal ions (*14*, *15*), and sequence specificity is also substantially enhanced (*14*). Indeed, while quantitative estimates vary, it seems clear that there is little binding selectivity when metal ions are absent (*14*, *16*−*18*). While catalysis proceeds efficiently with only Mg^{2+}, Mn^{2+}, or Co^{2+} (*19*), Ca^{2+} ions function as superb analogues of Mg^{2+} in the binding reaction, providing a convenient means of trapping a prereactive substrate complex in which the DNA is sharply bent by 50° at the center TA step of GATATC (*14*, *20*, *21*). Stopped-flow fluorescence and metal reconstitution experiments offer strong evidence that DNA cleavage by *Eco*RV requires at least two divalent metal ions per active site subunit (*19*, *22*). Interestingly, X-ray structures of uncleaved complexes show that the divalent metal ions bind at three distinct loci, bridging the scissile and 3′-adjacent DNA phosphates to several active site carboxylate groups (*15*, *21*, *23*−*27*). Further, another functionally important metal site specific to Mn^{2+} has been localized between the His71 imidazole ring and a phosphate group outside the GATATC sequence (*25*, *28*).

Two closely related mechanistic proposals, consistent with most biochemical data, invoke a transition state model featuring metal ions bound at each of the three loci near the scissile phosphates (Figure 1; *24*, *29*). This model is supported by pH−rate studies, which show that the Mg^{2+}-dependent phosphoryl transfer step follows a sharp bell-shaped curve with an optimum at pH 8.5, suggesting general base catalysis for the nucleophilic attack of hydroxide ion on the scissile phosphate, and general acid catalysis for protonation of the leaving 3′-O anion by a second ionized water (*29*). However, a weakness of the model is that all three divalent metal sites have not been simultaneously observed in any single structure (*25*, *26*). Structures of wild-type and base analogue *Eco*RV complexes have revealed Mg^{2+}, Mn^{2+}, or Ca^{2+} binding in sites II and III [refs *15*, *21*, and *23* and this work (Figure 1)], while Mg^{2+}, Mn^{2+}, or Ca^{2+} occupies sites I and II in structures of the T93A mutant and of a 3′-phosphorothiolate DNA analogue (*24*, *25*). However, there are no examples of pre-transition state ternary complexes in which metals are observed to bind in all three sites or in which the directly interacting metals in sites I and III are simultaneously present. Further, there are no biochemical data that distinguish between the participation of two versus three metal ions in facilitating catalysis. An alternative model that is also consistent with all biochemical data invokes only two metal ions in the catalytic event, and postulates a conformational change of the scissile phosphate to move it more deeply into the active site cleft. This local rearrangement has been observed in unrestrained molecular dynamics calculations (*30*).

It is clear that a detailed description of the near-attack conformation which precisely locates all metals, and in which hydroxide ion is poised to attack in-line at the tetrahedral ground state scissile phosphate, is still lacking. In addition, while the carboxylates at Asp90, Asp74, and Glu45 are highly likely to play structural roles in ligating metal ions, the catalytic role of the key Lys92 residue is less clear. Lys92 is conserved among a subset of restriction endonucleases, and its mutation to alanine produces a 10^5-fold reduction in the catalytic rate which is not improved in Mn^{2+} reactions (*26*, *31*). The amine group is positioned to play the role of a general base catalyst in accepting the proton ionized from the nucleophilic water, but there are no direct data to substantiate this hypothesis (*29*). An alternative role in stabilizing the attacking hydroxide while remaining in the protonated state seems to be equally likely. Attempts to reconstitute the activity of the K92A mutant with a series of exogenous amines varying in basicity were not successful in resolving this ambiguity (*26*).

An important limitation in the crystallographic analysis of *Eco*RV ternary complexes has been that the best-diffracting triclinic crystal form (in which all high-resolution analyses have so far been carried out) traps a DNA conformation in which the minor groove at the scissile phosphates is not fully opened (*32*). The structures determined in this lattice offer highly detailed views of the active site solvent environment, but the packing forces block catalytic activity in the crystal (*23*). Unfortunately, the only crystals in which activity can be measured *in situ* diffract to just 3 Å resolution and are thus also not optimally suited to studies of the catalytic mechanism (*33*). To address this limitation and to further explore crystallographic approaches to elucidating the reaction trajectory, we present four new structures of *Eco*RV mutants K38A and K92A bound in both prereactive and postreactive complexes with DNA and metal ions, at resolutions between 1.5 and 2.1 Å. In particular, the K38A postreactive structure was determined in two different crystal forms, revealing a common, novel conformation for the scissile phosphates that helps resolve significant differences among previously proposed two- and three-metal mechanisms. Further, structures of the K92A enzyme reveal a bound monovalent cation at the position of the lysine amine group. This suggests that the active site environment favors a positive charge at this position, helping to elucidate the role of this conserved lysine in catalysis.

Table 1: X-ray Data Collection and Refinement Statistics

	K92A−DNA−Mg^{2+}	K92A−DNA−Mn^{2+}	K38A−DNA−Mn^{2+}	K38A−DNA−Mn^{2+}
data set name	K92AMG	K92AMN	K38AMN1	K38AMN2
DNA	5′-CAAGATATCTT	5′-CAAGATATCTT	5′-AAAGATATCTT	5′-AAAGATATCTT
space group	*P*1	*P*1	$P2_1$	*P*1
cell dimensions	47.4 Å, 48.7 Å, 63.4 Å, 97.1°, 108.8°, 107.3°	47.8 Å, 49.1 Å, 63.7 Å, 96.9°, 108.9°, 107.1°	63.7 Å, 58.7 Å, 82.1 Å, $\beta = 107.7°$	47.7 Å, 48.6 Å, 63.5 Å, 96.7°, 108.9°, 107.3°
resolution (Å)	1.8	2.15	2.1	1.5
total no. of observations	127582	46123	103703	161152
no. of unique observations	64611	25244	33633	81312
completeness (%)	94.7 (90.1)	91.2 (89.7)	99.2 (98.1)	93.4 (92.3)
I/σ	2.3 (2.0)	3.8 (2.0)	4.7 (1.9)	9.5 (2.0)
multiplicity	2.0	1.8	3.1	2.0
R_{merge} (highest-resolution shell)[a] (%)	3.7 (32.4)	8.9 (30.7)	10.9 (35.7)	6.9 (32.7)
R_{cryst}[b] (%)	19.7	21.3	20.1	21.4
R_{free}[c] (%)	26.1	25.4	26.2	25.4
overall *B*-factor (Å^2)	30.0	42.2	32.8	32.8
rmsd for bonds (Å)	0.012	0.018	0.021	0.018
rmsd for angles (deg)	2.02	1.91	2.01	1.91
no. of waters	303	152	385	371
no. of metals	2 Mg^{2+}, 2 Na^+	6 Mn^{2+}	7 Mn^{2+}	9 Mn^{2+}

[a] $R_{merge} = (\sum_h \sum_i |\langle F_h \rangle - F_{hi}|)/\sum_h F_h$, where $\langle F_h \rangle$ is the mean structure factor magnitude of *i* observations of symmetry-related reflections with Bragg index *h*. [b] $R_{cryst} = (\sum_h \sum_i ||F_{obs}| - |F_{calc}||)/\sum |F_{obs}|$, where F_{obs} and F_{calc} are the observed and calculated structure factor magnitudes, respectively. [c] R_{free} is calculated with removal of 10% of the data as the test set, followed by simulated annealing refinement of the final model.

MATERIALS AND METHODS

Preparation of EcoRV Endonuclease Mutants. Oligonucleotides were purchased from IDT (Coralville, IA), and enzymes were purchased from New England Biolabs except where noted. The K38A mutant was prepared as previously described (*15*). The K92A mutant was prepared by the overlap extension PCR method using two amplifications and one extension reaction (*34*). Transformations of the ligated plasmid were performed by a rapid method as described previously (*35*). The template for each mutagenesis reaction consisted of a mixture of the expression plasmid *p*BSRV encoding the wild-type *Eco*RV gene together with an ampicillin resistance marker (*36*), and the *p*MetB plasmid encoding the *Eco*RV methyltransferase and kanamycin resistance genes (*37*). For all mutants, plasmid DNA was isolated from transformants, and the sequences of the genes were verified in their entirety.

Purifications of Enzymes and DNA Substrates. Wild-type and mutant *Eco*RV enzymes were expressed in *E. coli* strain MM294 (*endI*$^-$, *pro*$^-$, *thi*$^-$, $r_k^- m_k^+$), purified to homogeneity by a two-column procedure, and stored at a high concentration as an ammonium sulfate slurry, as described previously (*15*, *21*). No modifications to the purification protocol were necessary for either mutant. The purity of the enzymes is estimated to be ≥99% based on analysis of Coomassie-stained polyacrylamide gels. The oligodeoxynucleotides used in cocrystallizations were the self-complementary 11-mers 5′-CAAGATATCTT (K92A mutant structures K92AMG and K92AMN, Table 1) and 5′-AAAGATATCTT (K38A mutant structures K38AMN1 and K38AMN2). Each substrate possesses a single-base 5′-A or 5′-C overhang. Oligonucleotides were purified by HPLC,[1] mixed at equimolar concentrations, annealed by a heating and slow-cooling protocol, lyophilized, and stored at −20 °C until they were ready for use.

Crystallization and X-ray Structure Determinations. The K92A mutant was prepared by resuspending the ammonium sulfate slurry at 10 mg/mL in a buffer containing 10 mM HEPES (pH 7.5), 100 mM NaCl, 1 mM EDTA, and 0.1 mM DTT, followed by exhaustive dialysis against this buffer. The K38A protein was prepared by an identical procedure except that the concentration of NaCl was 250 mM. For cocrystallization trials, the 11-mer duplex oligodeoxynucleotides were brought to a concentration of 10 mg/mL in 50 mM Tris (pH 7.5) and 1 mM EDTA. Cocrystals of *Eco*RV K92A complexed with DNA and Mg^{2+} were grown by vapor diffusion from solutions containing 17% PEG 4K, 0.1 M sodium potassium tartrate, 50 mM $MgCl_2$, 0.1 M HEPES (pH 7.5), and 10 mg/mL protein with a 2:1 DNA:protein molar ratio (final conditions). Cocrystals of K92A containing Mn^{2+} were then prepared by soaking these crystals exhaustively in 25% PEG 4K, 0.3 M NaCl, and 0.1 M HEPES (pH 7.5), followed by a 1 h soak in 25% PEG 4K, 0.3 M NaCl, 50 mM $MnCl_2$, and 0.1 M HEPES (pH 7.5). Cocrystals of *Eco*RV K38A complexed with DNA and Mn^{2+} were grown by vapor diffusion from solutions containing 20% PEG 4K, 0.15 M NaCl, 50 mM $MnCl_2$, and 0.1 M HEPES (pH 7.5) (final conditions). Crystallizations of K38A under these conditions gave rise to two distinct crystal forms, and the data sets collected from those forms were designated K38AMN1 and K38AMN2 (Table 1).

All crystals were cryoprotected with a solution containing 25% PEG 4K, 0.1 M HEPES (pH 7.5), 0.3 M NaCl, and 30% glycerol, followed by flash-freezing in a stream of nitrogen gas at 100 K. X-ray diffraction amplitudes were measured on an R-AXIS IIC area detector mounted on a Rigaku RU-200 rotating anode generator (data sets K92AMN and K38AMN2), or using synchrotron radiation at SSRL beamline 7-1 (K92AMG) or SSRL beamline 9-1 (K38AMN1). Determinations of the orientation matrix and integration, scaling, and merging of data were performed with MOSFLM (*38*) and SCALA (*39*). Both structures of K92A and the triclinic structure of K38A (Table 1) were phased using the

[1] Abbreviations: HPLC, high-pressure liquid chromatography; DTT, dithiothreitol; PEG, polyethylene glycol.

*Eco*RV−DNA cocrystal structure previously determined in space group *P*1 (1RVA), with all solvent molecules and the side chains of Lys92, Asp90, Asp74, Glu45, Asp36, and Lys38 from both subunits removed from the initial model. The monoclinic structure of K38A (K38AMN1, Table 1) was determined by molecular replacement using XPLOR (*40*) and the wild-type *Eco*RV dimer structure (1RVA) as the search model. XPLOR (*40*) was used for early stages of refinement, while later stages were performed with CNS (*41*). For model building, CHAIN (*42*) and XtalView (*43*) were used.

Coordinates have been submitted to the Protein Data Bank and are listed as entries 1SUZ (K92AMG), 1SX8 (K92AMN), 1STX (K38AMN1), and 1SX5 (K38AMN2).

RESULTS

High-resolution X-ray crystallography of mutant enzymes can provide a level of detailed insight into functionally relevant structural transitions that is not possible with any other approach. We selected the K92A and K38A mutants of *Eco*RV as candidates to reveal such novel insights into the catalytic mechanism, based on their functional properties and positions in and adjacent to the active site. While Lys92 is very important for catalysis, its possible roles in providing general base catalysis and electrostatic stabilization in the unprotonated and protonated forms, respectively, have not been distinguished. Lys38 is located on the periphery of the active site cleft on a mobile loop that emanates from the opposing subunit of the dimer (Figure 2). While mutation of Lys38 to methionine or alanine decreases the rate of catalysis by 10^3-10^4-fold (*44*), double mutants combining K38A or K38M with substitution of the nearby Asp36 with asparagine are improved catalysts with activities of up to 2% of that of wild-type *Eco*RV (*26*). Lys38 is positioned some 8−10 Å from the scissile phosphate; its kinetic properties in conjunction with those of Asp36 suggest a role in modulating the electrostatic environment of the active site cleft. Further, while Lys38 is poorly ordered in substrate complexes, the positively charged amine group directly contacts two oxygens of the scissile phosphate in the wild-type product complex, suggesting a possible additional role in facilitating the later steps of the cleavage reaction.

Structures of EcoRV K92A Bound to Cognate DNA and Metal Ions. Crystals of the K92A mutant bound to an 11-mer duplex DNA containing the cognate GATATC site and Mg^{2+} ions grew in a triclinic space group isomorphous with that of the wild-type enzyme and other modified complexes (*15*, *21*, *23*−*27*). Crystals of this mutant bound to the same DNA substrate and Mn^{2+} ions were prepared by soaking the preformed K92A−DNA−Mg^{2+} crystals in solutions lacking Mg^{2+} and containing Mn^{2+} ions (see Materials and Methods). Crystals were cryoprotected, flash-frozen, and maintained at 100 K during data collection to prevent radiation decay. The crystals diffract to 1.8 and 2.15 Å for the Mg^{2+} and Mn^{2+} complexes, respectively, and refine with good agreement to the diffraction data while maintaining tight stereochemical constraints (K92AMG and K92AMN, Table 1). The two K92A structures are very similar to each other and to that of wild-type *Eco*RV bound in binary (with DNA) and ternary complexes in this crystal form. Superposition of main chain atoms among the core DNA-binding domains of K92A and wild-type monomers [comprising 122 amino acids (*21*)] yields rms deviations between 0.20 and 0.25 Å, within the coordinate errors. These superpositions also show that there are no global quaternary structure differences in the K92A mutant as compared to native *Eco*RV. This is in contrast to structures of the E45A and T93A mutants in the same crystal form, each of which exhibited significant global rearrrangements involving rotation of the two monomer DNA-binding domains apart by 2−3° (*24*, *26*). In both K92A structures, electron density for the DNA is strong and continuous across the scissile phosphates, indicating that a substrate complex with intact duplex DNA has been trapped in each case (Figure 3). Although the crystallization conditions support catalysis by *Eco*RV, no cleavage is observed because of the highly attenuated activity of this mutant (*26*, *31*).

The K92AMG and K92AMN structures exhibit overall DNA conformations very similar to each other and to that of the wild type, as well as an identical position of the scissile phosphate with respect to the active site in both subunits. The scissile phosphate is shifted inward toward the active site by ∼1 Å as compared with structures of the wild-type binary enzyme−DNA complex, and occupies a position identical to that of wild-type uncleaved ternary complexes [prepared by soaking Mg^{2+} or Mn^{2+} ions into preformed crystals (where cleavage is not observed in this triclinic space group) or by cocrystallization with inactive Ca^{2+} ions (*21*, *23*, *27*)]. In all structures, the center TA step of GATATC is sharply bent into the major groove, with roll angles of approximately 50° at this position. Except for small differences in the metal ion ligation spheres between the two subunits in K92AMN (see below), both mutant structures are identical in each active site. Significant differences of 1−3 Å in sections of the protein chain near the active sites are found for a linker segment (linker II, amino acids 34−40) and the minor groove binding "Q-loop" (amino acids 66−71), among K92AMG, K92AMN, and wild-type *Eco*RV (Figure 2). However, differences of this magnitude are found among many *Eco*RV binary and ternary complexes and apparently reflect the greater flexibility of these segments, as also corroborated by relatively higher atomic *B*-factors in all structures. Thus, these movements are not correlated with the K92A mutation.

There is also no movement of the backbone at Lys92 in response to the mutation. Only one well-ordered water molecule binds in the position of the lysine side chain in each structure (Figure 4A), but an additional solvent molecule is also bound that we identify as a sodium ion (see below). In both K92A mutant structures, an adjacent section of the main chain at and adjacent to Thr106 shifts away by ∼0.5 Å in apparent response to the mutation (Figure 4A).

Soaking of wild-type *Eco*RV−DNA crystals in this lattice with Mg^{2+} or Mn^{2+} ions produced binding in only one subunit (*23*). However, in the cocrystallized K92AMG and K92AMN complexes, the metals bind in both active sites (Table 1). Six Mn^{2+} ions were localized in K92AMN, two of which bind between the His71 imidazole and a distal phosphate group in each subunit, as previously reported (*25*). The Mn^{2+} ions in the active sites occupy the previously described sites II and III (Figures 1, 2B, and 4). The site III metal, located directly on the scissile phosphate, features a coordination sphere containing five ligands at distances from 2.1 to 2.8 Å: one carboxylate oxygen from Asp90, both carboxylate oxygens from Asp74, the *pro*-S_p phosphate

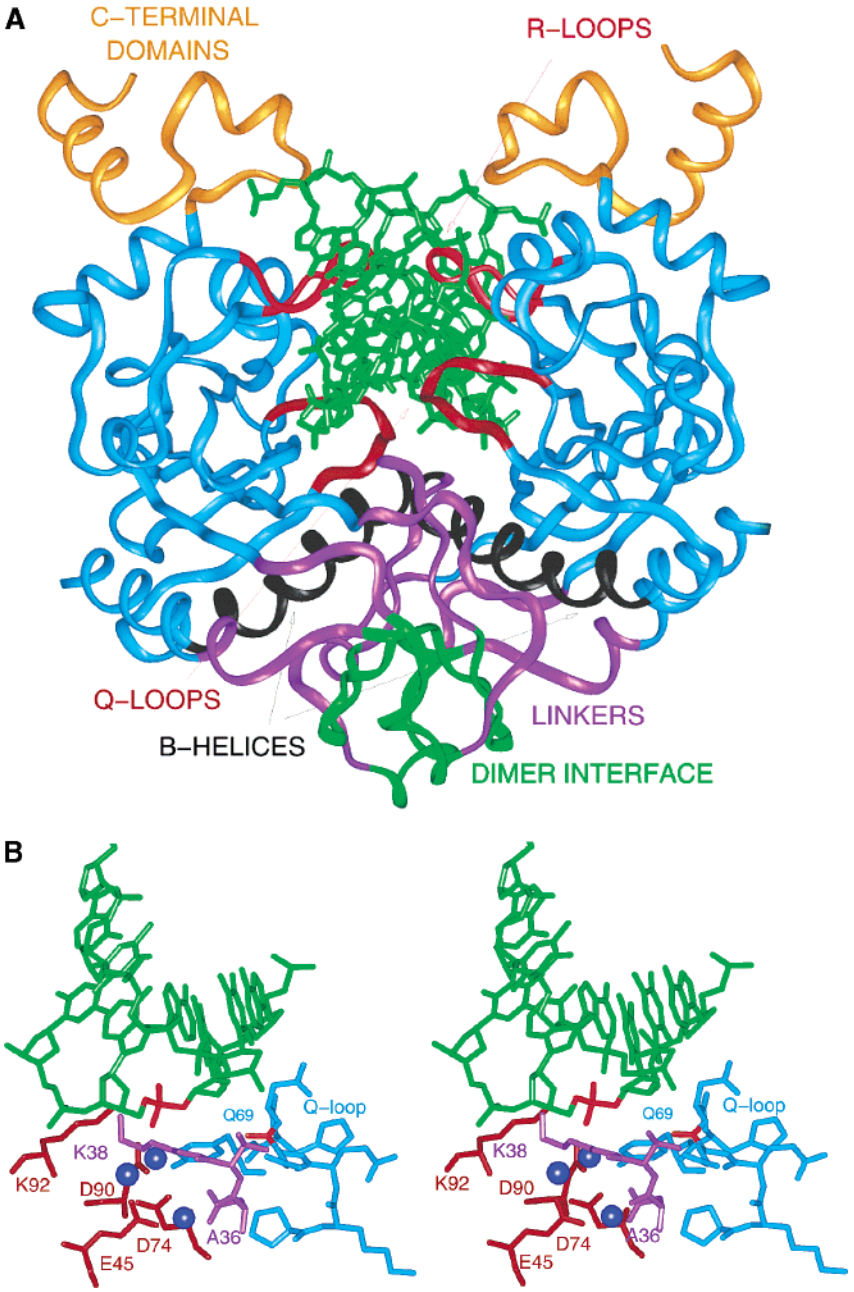

FIGURE 2: (A) Diagram of the wild-type *Eco*RV−DNA crystal structure showing the modular enzyme design (*33*). The DNA binding/catalytic subunits are shown in blue. Other regions of the enzyme are indicated with color-coded labels. The B-helices are key players in modulating DNA bending and are shown in black in each subunit. The R-loops (red) and Q-loops (maroon) bind in the major and minor grooves, respectively. (B) Divergent stereoview of the *Eco*RV active site environment in one monomer of the dimeric enzyme. The scissile phosphate of the DNA substrate at the top is shown in red. Key side chains of Lys92, Asp90, Asp74, and Glu45 are shown in maroon, while the linker region from the opposite monomer, containing the important Asp36 and Lys38 residues, is shown in purple. The Q-loop at right (blue) binds in the minor groove adjacent to the active site. The backbone carbonyl group of Gln69 within the Q-loop, which binds a metal ion in the product complex, is highlighted in red. Blue spheres denote the positions of the three divalent metals derived from the wild type (*23*) and modified complexes (*24*, *25*). Site III is directly on the scissile phosphate; site I is depicted to its left, and site II is more deeply buried in the pocket (see Figure 1).

oxygen, and one water molecule. By contrast, the Mn^{2+} ion in site II is bound to only three apparent ligands: Glu45, Asp74, and a water molecule. There are small differences in the Mn^{2+} ligand environments in the two subunits of K92AMN, apparently due to alternate rotamers that are adopted for the side chains of Asp90 and Glu45. The assignment of one Mn^{2+} ion to site II of one subunit is uncertain given lengthened inner sphere distances and a high *B*-factor of 72 Å^2.

The differences in divalent metal ligation for the two subunits of K92A observed in the presence of Mn^{2+} are not found when Mg^{2+} is bound. In this case, both active sites bind one Mg^{2+} ion (Figure 4). Confidence in the assignment of Mg^{2+} arises in part from the very high resolution of the structure (1.8 Å). Although scattering of Mg^{2+} is difficult to distinguish from that of water, in each active site the metal is bound to six inner sphere ligands in an octahedral arrangment with short distances consistent with Mg^{2+}−O

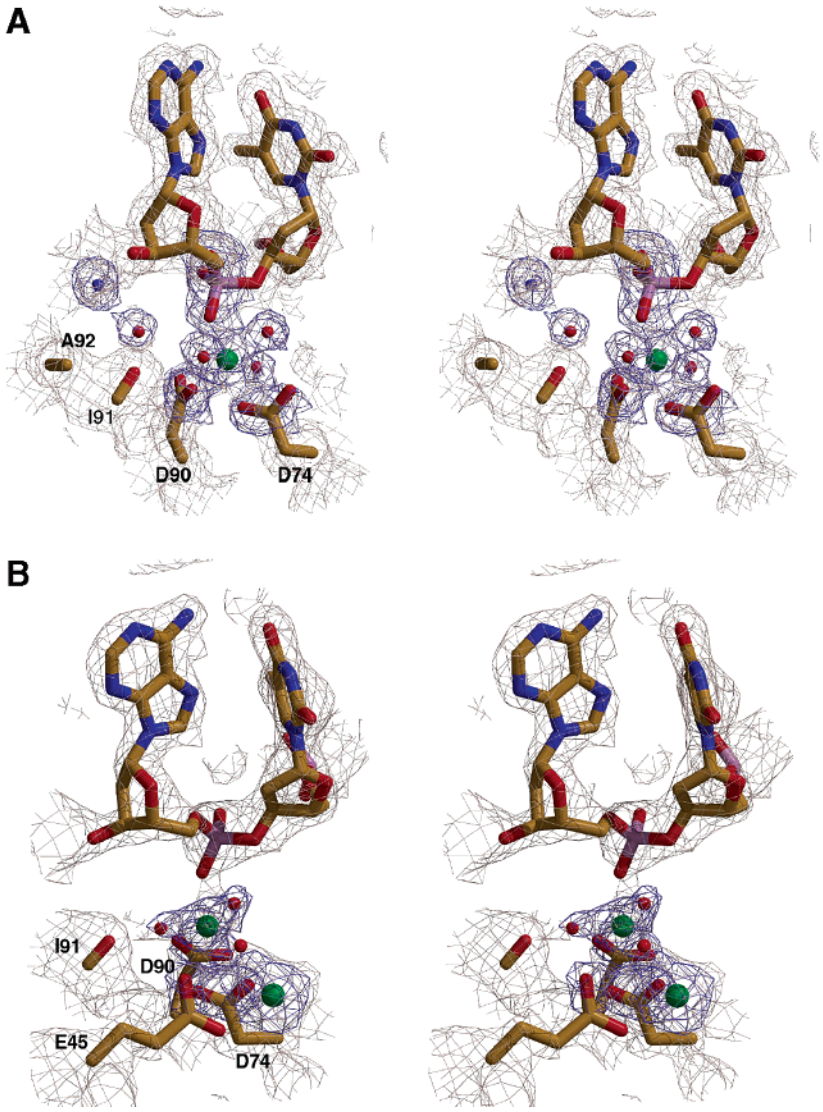

FIGURE 3: (A) Simulated annealing omit map in the active site region of subunit B in the structure of *Eco*RV K92A cocrystallized with cognate DNA and Mg^{2+} ions. The omitted groups comprise the scissile phosphate groups, the side chain carboxylates of Asp74 and Asp90, and the Mg^{2+} and Na^{+} ions with their closely associated waters. The structure was submitted to a simulated annealing refinement protocol with these groups removed, prior to calculation of maps. Shown is the electron density calculated from the omitted model phases and $2F_o - F_c$ coefficients at 1σ (light gray), superimposed on an $F_o - F_c$ map calculated form the same phases and displayed at 3σ (blue). (B) Simulated annealing omit map in the active site region of subunit B in the structure of *Eco*RV K92A bound to cognate DNA and Mn^{2+} ions. The omitted groups comprise the scissile phosphate groups, the side chain carboxylates of Asp74 and Asp90, and the Mn^{2+} ions together with associated water molecules. The simulated annealing $2F_o - F_c$ and $F_o - F_c$ maps are depicted as described for panel A.

bonds (*45*). Further, temperature factors for the Mg^{2+} ions refine to 19 and 22 Å^2 in the two subunits. The Mg^{2+} is found in site III (*24*) and is ligated to the side chains of Asp74 and Asp90, the *pro*-S_p oxygen of the scissile phosphate, and three water molecules.

Each active site in both K92A structures also reveals electron density that we interpret as an Na^{+} ion. Interestingly, the Na^{+} appears in a position only 2 Å from that occupied by the nitrogen of the K92 side chain in wild-type *Eco*RV. The electron density has been assigned as Na^{+} by the existence of five close ligands in the inner sphere to produce an approximate trigonal bipyramid geometry, and by observation of temperature factors during alternative refinements in which the electron density was modeled as either water, K^{+}, or Na^{+}. Modeling of the electron density with water results in *B*-factors of 2.0, while *B*-factors when modeled as K^{+} refine in the range of 58−61 Å^2 in the different subunits. By contrast, temperature factors ranging from 28 to 35 Å^2 were obtained when the electron density was modeled as Na^{+}. Further, while K^{+} ions were included in the crystallization buffer for growth of the Mg^{2+} cocrystals, they were removed when the crystals were soaked in Mn^{2+}-containing solutions (see Materials and Methods). The Na^{+} ion directly coordinates the *pro*-R_p oxygen of the 3′-adjacent phosphate group and may help shield the charge between the scissile and 3′-adjacent phosphates, which move closer than usual for B-form DNA because of the sharp DNA bending at the center TA step (Figure 5). We infer that this may be an important and previously unrecognized function of a protonated Lys92 side chain in the native enzyme.

Structures of EcoRV K38A Ternary Product Complexes in Alternative Lattice Environments. The *Eco*RV K38A mutant was cocrystallized with cognate DNA and Mn^{2+} ions under conditions similar to those that yielded crystals of K92A, but in this case, two distinct crystal forms were obtained. One crystal was found to be in the common triclinic

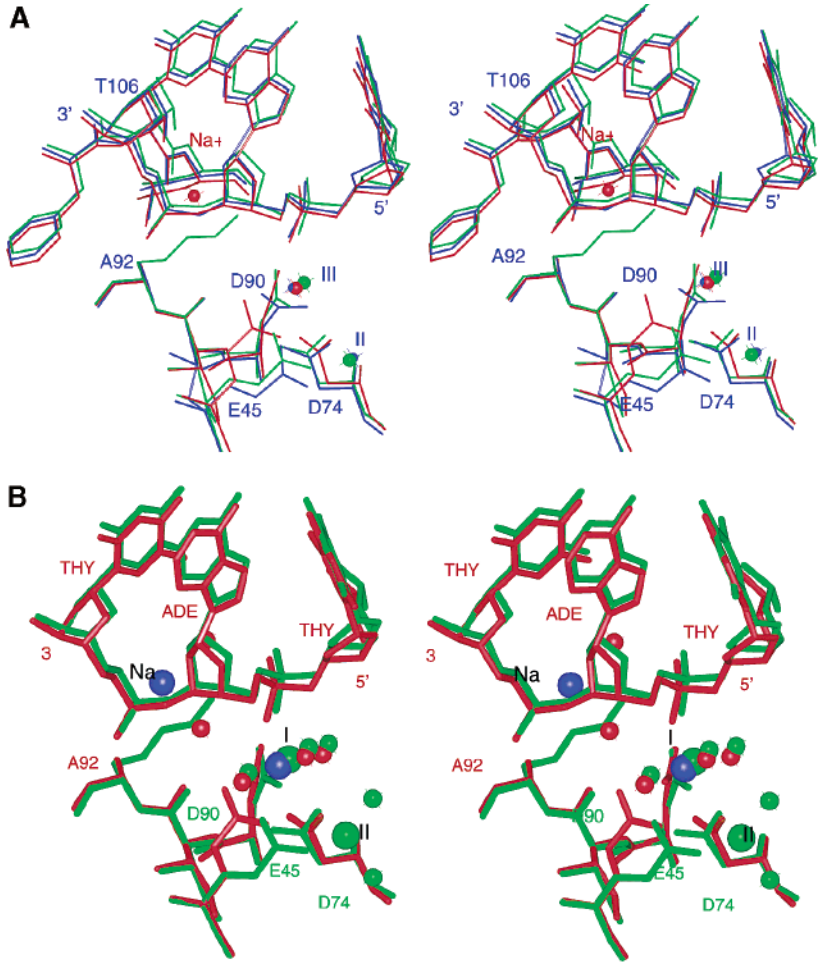

FIGURE 4: (A) Stereoview of the wild-type ternary *Eco*RV−DNA−Mg^{2+} complex (green), superimposed on the structures of *Eco*RV K92A cocrystallized with Mg^{2+} and Na^+ ions (red), and *Eco*RV K92A bound to Mn^{2+} ions (blue). Spheres denote the positions of metal ions. (B) Stereoview of the wild-type ternary *Eco*RV−DNA−Mg^{2+} complex (green), superimposed on the structure of *Eco*RV K92A cocrystallized with Mg^{2+} and Na^+ ions (red), in the active site of subunit B. The larger blue spheres represent the Na^+ ion and the Mg^{2+} ion (occupying site III) in the K92AMG complex; Mg^{2+} ions in sites II and III in the wild-type enzyme are shown in green. The smaller spheres represent water molecules in the inner spheres of these metals.

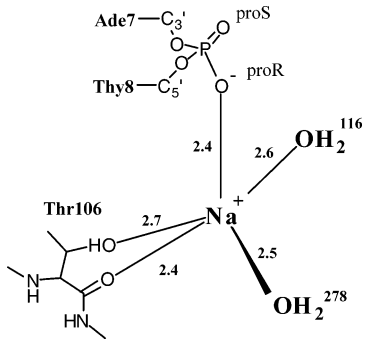

FIGURE 5: Interactions of the sodium ion in subunit B of the *Eco*RV K92A−DNA complex cocrystallized in the presence of Mg^{2+} and Na^+ ions. Inner sphere distances are indicated in angstroms. The phosphate indicated is that 3′ to the scissile phosphate at 5′-GATA*p*TC-3′. The identities of the inner sphere ligands for the Na^+ ion are identical in all four subunits of the K92A structures bound to Mg^{2+} or Mn^{2+}, and there are only small differences up to at most 0.4 Å in the ligand distances.

form isomorphous to those of the wild-type enzyme, K92A, and other modified *Eco*RV complexes (*15*, *21*, *23*−*27*). The second crystal, however, grew under identical conditions in a new monoclinic space group not previously characterized (K38AMN1, Table 1). This represents a fifth distinct crystal form of *Eco*RV bound to cognate DNA (*23*, *32*, *33*). The structure of K38A in this monoclinic lattice was determined by molecular replacement and refined to 2.1 Å resolution. Comparison of the K38A−DNA−Mn^{2+} crystal structures in the *P*1 and $P2_1$ lattices shows that there are no significant global differences in the tertiary or quaternary structure of *Eco*RV in the two forms. The rms deviation in the position of backbone atoms among the conserved monomeric cores, for the two structures of K38A and the wild-type enzyme, ranges from 0.23 to 0.32 Å, within the coordinate error. Both K38A structures show a very small difference of ∼1−1.5° in the relative spatial orientations of the two subunits, as compared to the wild type. This contrasts with the unchanged intersubunit orientation found for K92A, and is approximately half the magnitude of the rotation found previously for the E45A and T93A mutants (*24*, *26*). Both K38A structures also reveal two Mn^{2+} ions bound in similar positions in each subunit, as well as further Mn^{2+} ligated to His71 and His193 outside the active sites (Table 1).

In both K38A structures, the DNA is found cleaved in the crystal, in distinction to the uncleaved DNA found for K92A, and consistent with the significant retention of Mn^{2+}-dependent activity by this mutant [Figure 6 (*26*, *44*)]. While there are only small differences in most DNA helical

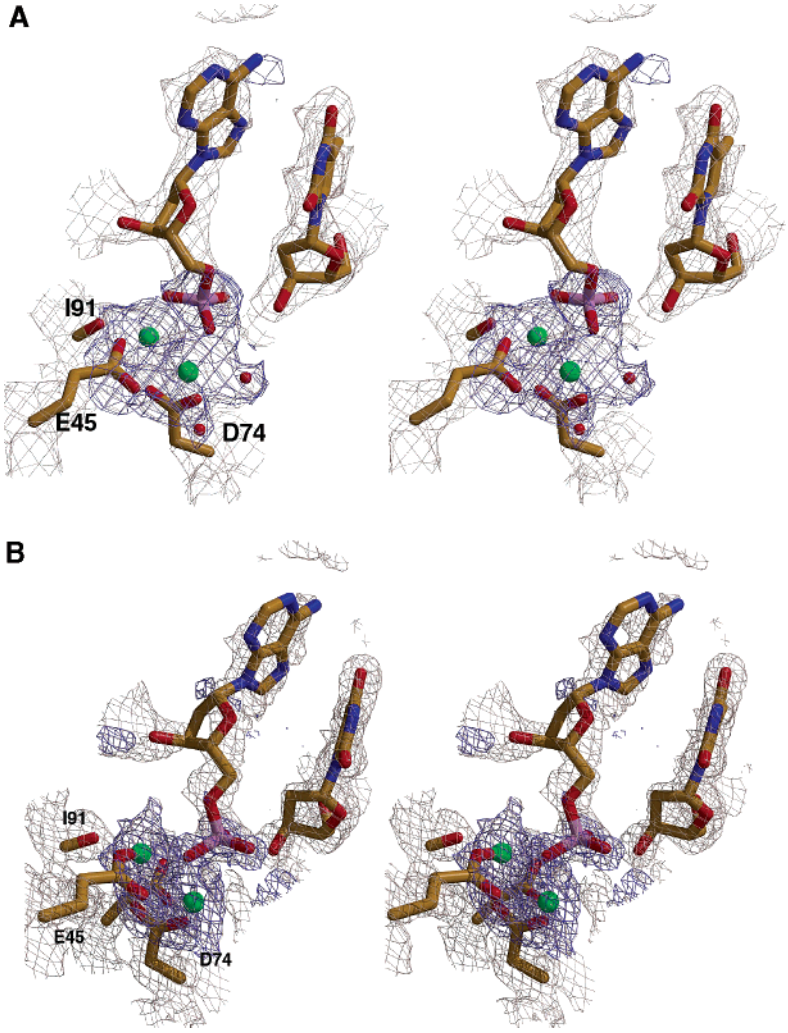

FIGURE 6: (A) Simulated annealing omit map in the active site region of subunit A in the structure of *Eco*RV K38A cocrystallized with cognate DNA and Mn^{2+} ions in space group $P2_1$ (structure K38AMN1, Table 1). The omitted groups consist of the scissile phosphates, side chain carboxylates of Asp90 and Asp74, and the Mn^{2+} ions and their closely associated waters. The simulated annealing $2F_o - F_c$ and $F_o - F_c$ maps are depicted as described in the legend of Figure 3. (B) Simulated annealing omit map in the active site region of subunit A in the structure of *Eco*RV K38A cocrystallized with cognate DNA and Mn^{2+} ions in space group $P1$ (structure K38AMN2, Table 1). The omitted groups and depictions of the maps are as described in the legend of Figure 3.

parameters among the two K38A product complexes and that of the analogous cleaved complex previously determined for wild-type *Eco*RV (*23*), the detailed conformation and divalent metal ligation at the scissile phosphate are significantly altered. In the wild-type product complex, the adenine bases at the center TA step of GATATC exhibit cross-strand stacking, and the scissile phosphate is located 3.8−4.0 Å deeper in the active site cleft than in the uncleaved ternary complex (Figure 7). Two Mg^{2+} ions were found in this wild-type complex: one at a position between sites I and II in the uncleaved state and the second some 6 Å distant on the far side of the cleft. This second Mg^{2+} ion in the wild-type complex interacts with the backbone carbonyl oxygen of Gln69 and several water molecules, in addition to the cleaved phosphate group.

By contrast, superpositions show that in K38A the conformation of the DNA at the center step more closely resembles the uncleaved state, because there is no cross-strand stacking of the adenine bases as observed in the wild-type product complex (Figure 7A). In K38A, two metal ions in each subunit of the cleaved K38A ternary complexes are positioned quite close to the metal sites in the uncleaved *Eco*RV structures (Figure 7B). Further, the phosphate group in these structures is found 2.1−3.5 Å from its position prior to cleavage, closer to its location in the cleaved (wild-type) state. A possible rationale for the novel position and metal ligation of the scissile phosphate in K38A is that, in the wild-type product complex, the Lys38 side chain interacts directly with this group (Figure 8D). Thus, mutation of Lys38 to alanine has disrupted interactions normally made in the product complex, allowing trapping of a new conformation which appears to represent an intermediate stage in the reaction trajectory. The phosphorus in the mutant structures is found 1.1−2.9 Å from its position in the cleaved wild-type structure. A set of distinct conformers for the scissile phosphate and adjoining linkages is observed in the four structures of K38A, which represent the two monomeric subunits in each of the triclinic and monoclinic space groups (Figure 9). The multiple positions found for the scissile phosphate in K38A may reflect the flexibility of this group in the mutant postcleavage complex lacking the stabilizing ionic interaction provided by Lys38. Despite the variability in the position of this cleaved 5′-product, the liberated 3′-OH group and most of the inner sphere interactions of the

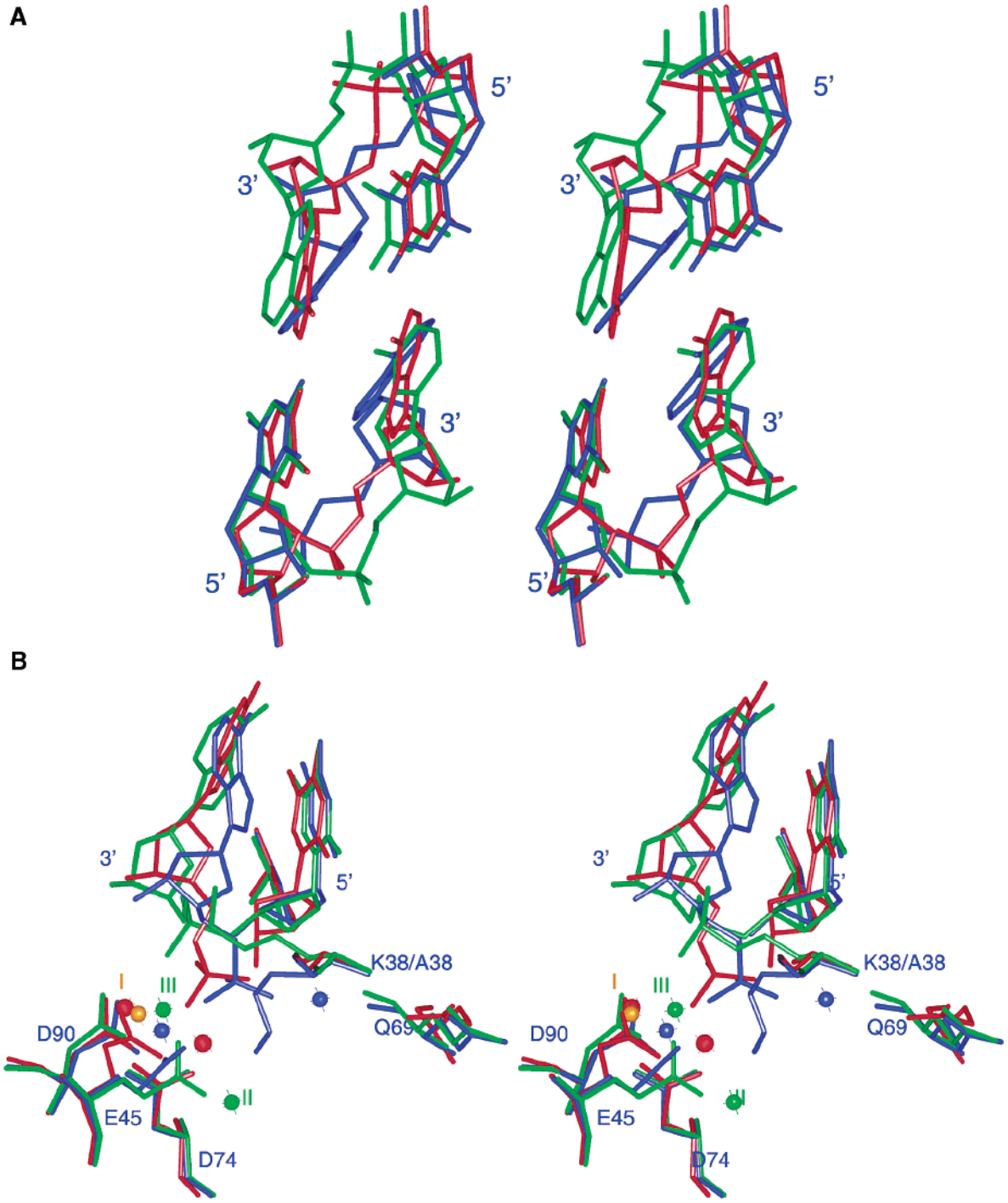

FIGURE 7: (A) Stereoview of the wild-type ternary *Eco*RV−DNA−Mg^{2+} complex (green), superimposed on the structures of the wild-type product complex (blue) and the K38A product complex (red). The K38A structure depicted is determined in space group $P2_1$ (K38AMN1, Table 1). Only the wild-type product complex features cross-strand adenine stacking at the center TA step. (B) Stereoview of the structures depicted in panel A, depicting features of the active site. Mg^{2+} ions bound at sites II and III in the wild-type uncleaved structure are shown as green spheres; blue spheres show the position of Mg^{2+} ions in the wild-type product complex (*23*), while red spheres show metal positions in K38A. The orange sphere is a metal ion bound in site I, taken from the structure of *Eco*RV bound to a DNA analogue (*25*). Lys38 in the uncleaved wild-type structure points upward toward the opened bases at the center TA step, but this side chain is often disordered in uncleaved *Eco*RV crystal structures.

metal ions are conserved among the four K38A active sites (Figure 9).

Both the position and inner sphere environment of the Mn^{2+} ion bound in site I of the two K38A structures are highly similar to those of the divalent metal (Mg^{2+}, Mn^{2+}, or Ca^{2+}) occupying site I in four high-resolution uncleaved ternary complexes of the T93A mutant or the wild-type enzyme bound to a phosphorothiolate DNA analogue (*23*, *25*). In each of these six structures, inner sphere interactions are made with a carboxylate oxygen of Asp74 and with the backbone carbonyl oxygen of Ile91 (Figure 8). A third common contact is made most often with the side chain carboxylate of Glu45, although this interaction is either absent (>3.2 Å) or replaced by a contact with Asp90 in several subunits. In the uncleaved structures, the remaining inner sphere positions at site I are occupied by water

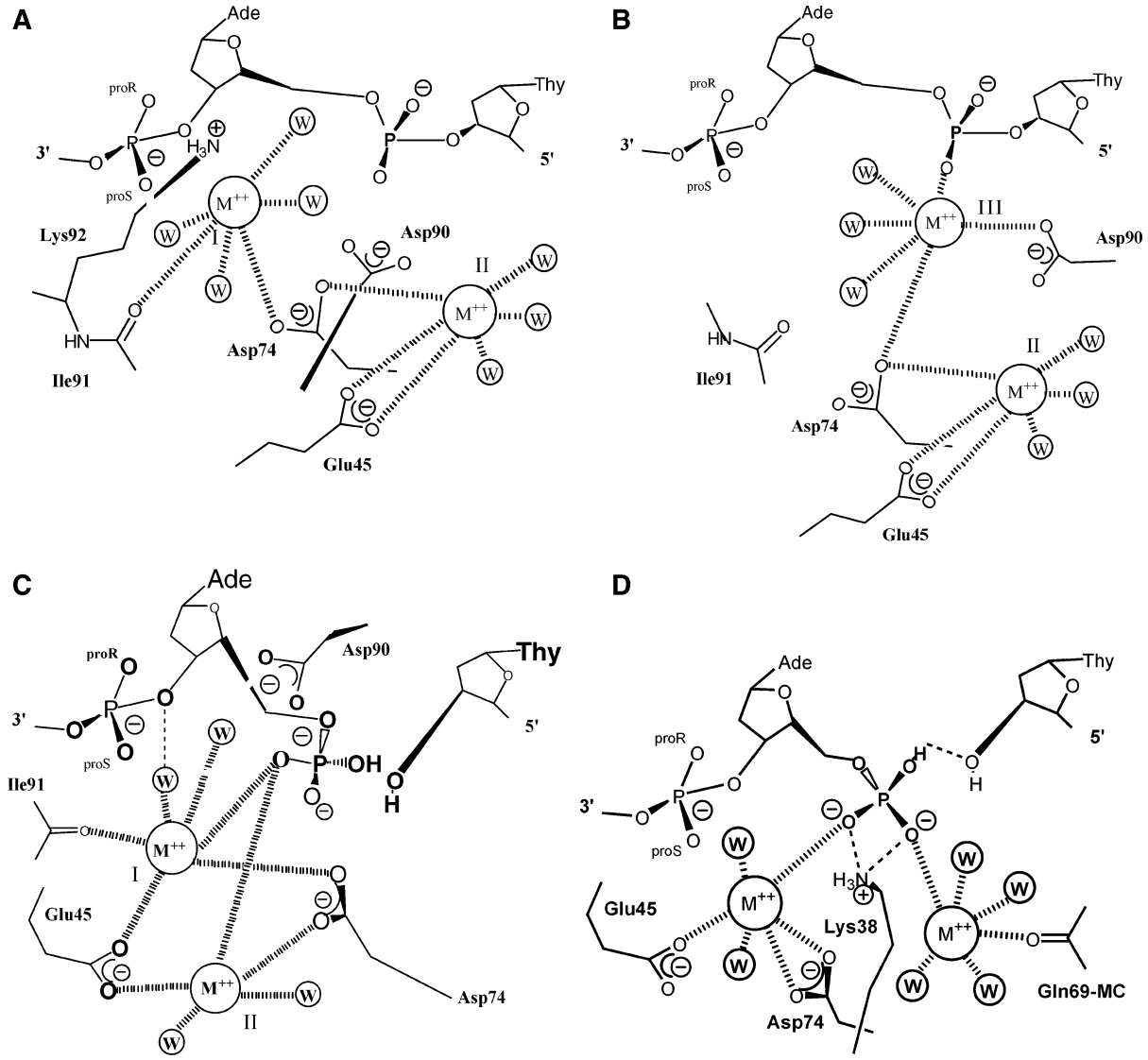

FIGURE 8: Schematic diagrams of metal ligation in *Eco*RV substrate and product complexes. (A) Uncleaved *Eco*RV−DNA complex indicating metal binding in sites I and II, as found in the structures of *Eco*RV T93A bound to Ca^{2+} and *Eco*RV bound to a 3′-*S*-phosphorothiolate DNA analogue in the presence of Mg^{2+}, Mn^{2+}, or Ca^{2+} (*24*, *25*). (B) Uncleaved *Eco*RV−DNA complex indicating metal binding in sites II and III, as observed in the wild-type ternary complex (*23*) and in structures of the K92A mutant (Figures 3 and 4). (C) Metal ion ligation seen in the cleaved structure of *Eco*RV K38A bound to DNA and Mn^{2+} ions, in subunit A of the structure determined in space group *P*1 (Table 1). Differences in metal ion ligations in the four K38A active sites are discussed in the text (see also Figure 9). (D) Metal ion ligation seen in the cleaved structure of *Eco*RV bound to product DNA duplexes in the presence of Mg^{2+} ions (*23*). In all panels, hatched lines denote inner sphere metal ligation and dotted lines hydrogen bonds.

molecules. However, in the K38A product complex, the site I metal also directly ligates at least one oxygen atom of the cleaved phosphate. In subunit B of the *P*1 structure, two inner sphere contacts with the scissile phosphate are made with site I. This arises because the phosphate in this subunit adopts an outlying position, which is correlated with an alternate rotamer for Glu45 (this subunit is also the only one in which the site I metal interacts with Asp90). On the basis of superpositions on core backbone elements in each subunit, the site I metals in the K38A subunits are displaced just 0.7−0.8 Å from their positions in uncleaved complexes (Figure 7B) (in *P*1 subunit B, this distance is increased to 1.2 Å).

The second metal site in K38A is displaced 2.0−2.3 Å from site II of uncleaved complexes. However, the inner sphere ligation of the metal ions is nonetheless quite similar. In each subunit of both K38A structures, the Mn^{2+} ion in site II ligates carboxylate oxygen atoms from both Asp74 and Glu45, as found in the uncleaved state (Figure 9). In several cases, two carboxylate oxygens of Glu45 are ligated. The site II metal ion also binds the scissile DNA phosphate, although in the outlier *P*1 subunit B active site, the distance between the atoms is too great to be favorable for the inner sphere environment. In this subunit, two oxygens from the scissile phosphate bind the site I metal ion. By contrast, in subunit A of the structure determined in space group $P2_1$ ($P2_1$A), distinct phosphate oxygens bind the metals in sites I and II, respectively. In the other two subunits (*P*1A and $P2_1$B), the same phosphate oxygen chelates both metal ions. The two metal ions are found 3.4−3.8 Å apart in the four K38A active sites, similar to the distance (3.9 Å) separating divalent metals in the classic two-metal ion mechanism [Figure 9 (*9*, *10*)]. In contrast to the 5′-phosphate, the 3′-

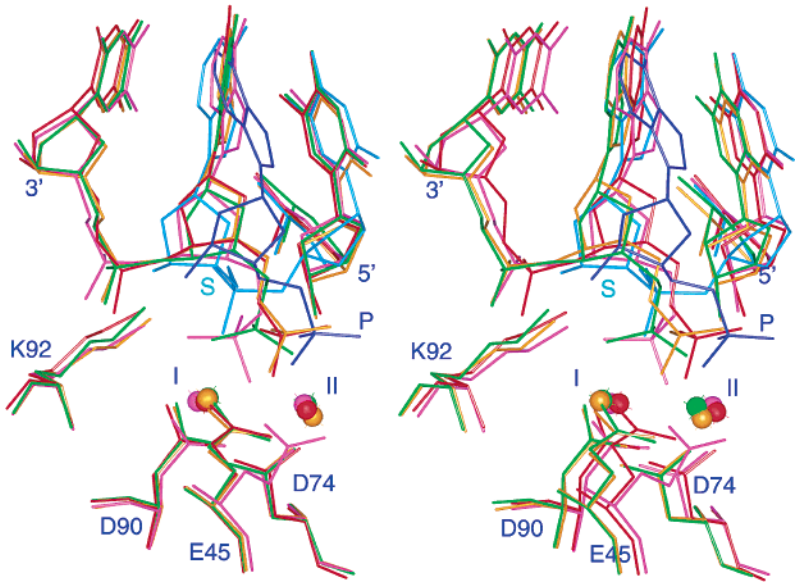

FIGURE 9: Superposition of four active site subunits from the two K38A dimers (K38AMN1 and K38AMN2, Table 1). The subunits are color-coded as follows: *P*1 subunit B (P1B) in purple, $P2_1A$ in green, $P2_1B$ in red, and *P*1A in orange. For comparison, the positions of the scissile phosphates in the wild-type substrate (light blue, S) and product (dark blue, P) are also shown. The K38A cleaved phosphates adopt configurations intermediate between the wild-type cleaved and uncleaved structures. Bound metal ions are in nearly the same positions in all four subunits despite the variability in phosphate position. The metal sites are denoted sites I and II.

product is displaced by only ~1 Å from its uncleaved position (Figure 7B), and a hydrogen bond between the two products is retained in all wild-type and mutant structures.

DISCUSSION

Induced Fit Conformational Changes in the EcoRV−DNA Complex. Previously, a set of detailed local and global conformational changes essential to the precise juxtaposition of reactive moieties in the *Eco*RV active site has been described (*32*, *33*). The *Eco*RV dimer populates different quaternary structures in its unliganded state, and the two catalytic subunits undergo an approximately 20° rotation about an axis roughly parallel to that of the DNA, upon binding of this substrate (*21*). The global rearrangement of protein quaternary structure is accompanied by sharp bending of the DNA by approximately 50° into the major groove at the center TA step of GATATC. Polypeptide segments binding directly in the DNA grooves also become ordered in these transitions (R-loops and Q-loops, Figure 2), as does the entire 29-amino acid C-terminal subdomain. The widened DNA minor groove is then essential for accommodating divalent metal ions adjacent to the scissile and 3′-adjacent phosphates, setting up an inner sphere water molecule from one metal for ionization and nucleophilic attack on phosphorus.

X-ray crystallography of the *Eco*RV−DNA complex in different crystalline environments was used to track the *Eco*RV conformational transitions through a 50% change in DNA bending angles (*32*). On the basis of these data, we proposed a DNA bending mechanism involving two distinct steps. First, an initial shallow bending is generated by asymmetric neutralization of the DNA phosphates on one face of the duplex, via interaction of these moieties with the positively charged C-terminal subdomain from each subunit. This initial bending, which may occur at both cognate and nonspecific sites, is followed by the sharp, specific bend triggered when the GATATC sequence is recognized in the major groove by the enzyme R-loops. The crystal structures show that greater DNA bending into the major groove is facilitated by improved protein−DNA complementarity in the minor groove, and that direct force may be exerted by contacts of Thr37, at the extreme N-termini of the B-helices (Figure 2A), with the ribose sugar at the center thymine nucleotide of each ATC half-site. These contacts are proposed to drive a set of final conformational transitions in which the two B-helices translate by one turn with respect to each other, and the scissile phosphates are concomitantly pulled more deeply into the active sites.

The crystal structures of the *Eco*RV K92A mutant presented here suggest now that DNA bending may be further facilitated by a monovalent positive charge located between the scissile and the 3′-adjacent phosphate groups (Figure 4). This suggestion is based on our finding that binding of a sodium ion very close to the same location compensates for removal of the Lys92 amine group in the K92A mutant. Thus, the active site environment appears to favor a positive charge at this position, suggesting that the Lys92 amine is indeed protonated at the pH optimum of 8.5 for the phosphoryl transfer reaction (*29*). This may be crucial because in the *Eco*RV−DNA complex the distance between the scissile and 3′-adjacent phosphates is significantly shortened from the canonical B-DNA value of 7.0 Å to approximately 6.4 Å, indicating a more A-DNA-like conformation at this position. The decreased inter-phosphate distance demands a greater role for charge neutralization in facilitating the rearrangement, consistent with theoretical and experimental considerations suggesting an important role for inter-phosphate repulsions in maintaining DNA stiffness (*46*). Interestingly, previous experiments in several laboratories have suggested that an important role for divalent cations is to shield the close approach of negative charges on the DNA phosphates and active site amino acid carboxylates, and that this role is likely crucial in facilitating the very tight, specific metal-dependent binding by many restriction endonucleases

(*14*, *47*, *48*). In *Eco*RV in particular, additional charge neutralization via specific placement of a monovalent positively charged lysine then may have additional importance in the induced fit rearrangement steps that follow initial binding. Lys92 is not conserved among canonical type II restriction endonucleases, and this may be related to the absence of a common mechanism for DNA distortion upon binding. For example, *Bam*HI possesses a glutamate in the equivalent position (Glu113), and this enzyme cleaves its DNA target site without bending it (*49*).

Lys92 in *Eco*RV may form a key contact that helps to drive the sharp DNA bending, which is similar to the proposed role of Thr37 (*32*). Alternatively, the salt bridge formed by Lys92 may stabilize the fully bent state after its formation. If this is the case, then the role of Lys92 would be identical to that proposed for divalent metal ions, which also stabilize the bent DNA as shown recently by fluorescence resonance energy transfer experiments (*50*). In *Eco*RV, there is likely no binding site for divalent metal ions before the DNA bends (*21*, *33*), but their absence may result in very rapid "unbending" of the DNA rather than movement forward toward the transition state.

If Lys92 indeed remains protonated in the DNA complex, it would be unable to function as a catalytic base to abstract a proton from the attacking water molecule in the initial bond-forming reaction step, as previously hypothesized (*29*). Instead, the protonated Lys92 might have a different role in facilitating the chemical step that follows binding and induced fit, by helping to stabilize the orientation of the hydroxide ion prior to its nucleophilic attack (see below and refs *24* and *29*).

Pathway of Phosphoryl Transfer in the EcoRV Active Site. The structures of K38A cocrystallized with specific DNA and Mn^{2+} ions in both the *P*1 crystal and a new monoclinic form (Table 1) show that the DNA is cleaved. However, three features of the mutant structure suggest that, compared to the wild-type product complex, an intermediate state along the reaction trajectory has been trapped. First, the scissile phosphate in K38A is located at a position part way between that adopted in the intact and cleaved wild-type structures (Figures 7 and 9). This phosphate shift in the K38A mutant may arise from removal of the salt bridge with the Lys38 amine group, resulting in a conformation that resembles a state directly after the bond-breaking catalytic step. Second, DNA helical parameters at the center TA step for K38A more closely resemble those of the precleaved conformation. This is evident in the marked cross-strand adenine stack found in the wild-type product complex but not in either the K38A product structure or in uncleaved complexes (Figure 7A). Finally, in both subunits of each K38A structure, two Mn^{2+} ions bind directly to the released 5′-phosphate at positions near sites I and II in the precleaved complexes, again suggesting that a conformation immediately following cleavage is being visualized.

Together, these observations suggest that the K38A structures offer a reliable and novel view of the *Eco*RV active site at a stage immediately following the catalytic step. This permits formulation of a new catalytic model based on the inference that in the immediate pretransition state configuration, the scissile phosphate group and two divalent metal ions are found very close to these positions at sites I and II (Figure 10).

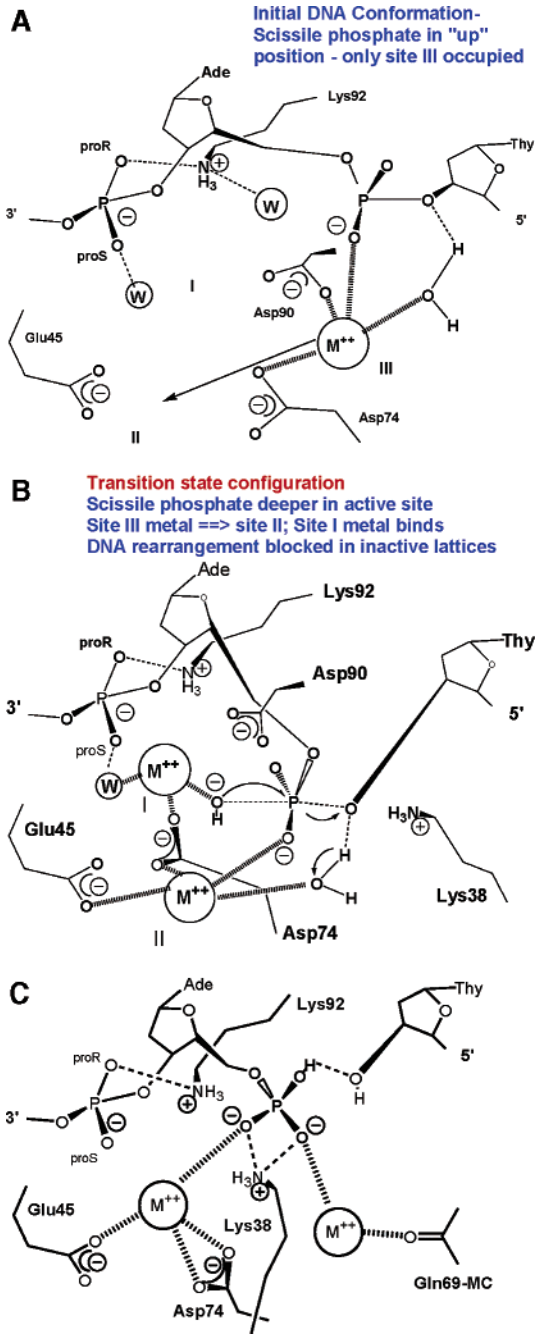

FIGURE 10: Two-metal ion mechanism involving three divalent metal sites. (A) A metal ion is shown bound in site III as visualized in structures of the wild-type enzyme and modified complexes bound to uncleaved DNA. Next, the metal ion shifts position to bind in site II, while maintaining its interaction with the scissile phosphate; this movement also allows a second metal ion to bind in site I. The rearrangement produces an intermediate, uncleaved conformational state (B) that may represent the immediate preattack configuration with metals bound in sites I and II. Cleavage then occurs, resulting in the product structure (C) in which one of the two metals (probably the metal in site II) is transported across the active site to bind the Gln69 carbonyl oxygen atom. The rearrangements after cleavage include adoption of the cross-strand adenine stack at the center TA step, which is visualized only in the wild-type product complex. The absence of the K38 side chain in the K38A structures results in trapping the cleaved structure in a conformer resembling that in panel B.

We suggest further that the structural pathway between initial substrate binding and the attainment of this near-attack conformation in which all moieties are properly poised for

catalysis utilizes all three divalent metal binding sites visualized in the uncleaved structures. In the first proposed step, a metal ion binds to site III directly at the scissile phosphate. This induces a roughly 1 Å movement of the DNA more deeply into the pocket, as shown previously by the comparison of binary (*Eco*RV−DNA) and ternary (*Eco*RV−DNA−M^{2+}) complexes (*23*). While site III is not occupied in the proposed transition state, we suggest that it is needed to facilitate the further conformational change in the scissile phosphate which pulls it deeper into the active site. It appears that it is this conformational change that is blocked in the crystalline environment of the *P*1 lattice in which all ternary complexes have so far been studied. The roughly 3 Å movement of the scissile phosphate group in this rearrangement is accompanied by movement of the site III metal ion such that it then occupies site II (Figure 10). This facilitates then the binding of a second metal ion to site I either directly following or concomitant with the conformational change. The metal ion transfer from site III to site II is consistent with the observation that sites I and III are never observed simultaneously, while sites I and II are found together in many uncleaved structures as well as in the cleaved K38A. In addition, there are several examples of structures in which site III is occupied, but sites I and II are not (*21*). Since a metal at site III is the only one that directly binds the scissile phosphate in uncleaved complexes, a role for it in the stereochemical pathway seems to be highly likely. With this model, the simultaneous metal occupancy of sites II and III observed in crystal structures does not represent a true intermediate, but rather an artifact arising from trapping of the complex in an inactive crystal lattice in the *P*1 crystal form.

Although no crystal structure of the scissile phosphate group ligating two metal ions in an appropriate catalytic geometry has been available until now, some aspects of this mechanism have been proposed before on the basis of the wild-type X-ray structures, as well as on findings that *Eco*RV requires at least two metal ions for DNA cleavage (*19*, *22*, *23*). In particular, stopped-flow studies monitoring *Eco*RV cleavage by tryptophan fluorescence showed that the reaction involves two Mg^{2+}-dependent steps that have distinct kinetic and thermodynamic dependencies (*22*). One metal ion is incorporated into the *Eco*RV−DNA interface in an initial rapid binding phase, giving fluorescence enhancement, but a subsequent hydrolytic/product release phase exhibiting a slow fluorescence decrease requires binding of a second metal ion. Thus, the intermediate proposed on the basis of the fluorescence experiments may correspond to the enzyme−DNA−M^{2+} complex with a metal ion either in site III or translocated to site II (Figure 9), while the second metal ion then subsequently binds to site I to initiate the slower catalytic step [k_{cat} for Mg^{2+}-dependent cleavage is a combination of both the phosphoryl transfer and product release steps (*22*)]. Occupancy of sites I and II places the metals in-line with the apical positions of the phosphate after the conformational rearrangement, with the site I metal generating the nucleophilic hydroxide ion, while the site II metal ion helps to neutralize the transition state while also ionizing a different water molecule to protonate the 3′-oxyanion. The finding that *Eco*RV exhibits a very sharp bell-shaped pH−rate profile with a maximum at pH 8.5 shows that there are two proton transfers in the catalytic step, consistent with a two-metal mechanism in which the leaving group is protonated by an ionizing water during the reaction, rather than being neutralized by direct ligation to a metal ion as proposed for the classic two-metal mechanism (*9*, *29*).

Because the K38A structures are determined in the cleaved state, it is not possible to definitively assign the precise ligation spheres of the metal ions in the pretransition configuration. However, it seems most likely that translocation of the site III metal ion together with the phosphate would retain the inner sphere contact of this metal ion on the *pro-S* oxygen. In the visualized product complex, this oxygen would then correspond to that ligating the metal ion bound near site II (Figures 7−9). The other two nonesterified oxygens on the cleaved phosphate then correspond to the *pro-R* oxygen and the attacking hydroxide ion, respectively. If there is minimal rearrangement directly after cleavage (but before a final conformational change; see below), then the site I metal might retain inner sphere contact with the attacking nucleophile. The remaining oxygen, which accepts a hydrogen bond from the 3′-product hydroxyl group in the K38A structures, then corresponds to the *pro-R* oxygen of the scissile phosphate prior to cleavage.

After cleavage of the scissile bonds through the action of the metals in sites I and II, a further conformational change to form the final product complex is required, including movement of the metal from site II to a position bridging the scissile phosphate with the backbone carbonyl group of Gln69 (Figure 10). We suggest that this final rearrangement after cleavage is promoted by the side chain of Lys38, and that the removal of this group in the K38A mutant is responsible for trapping the phosphate in the observed configuration. The K38A structures further suggest that the marked cross-strand stacking of the adenine rings observed in the wild-type product complex also occurs in the final conformational change after cleavage. Hence, this proposal invokes a significant postcleavage rearrangement in the ternary complex that might contribute to the slow rate of product release. Product release is fully rate-limiting for Mn^{2+}-catalyzed reactions (*30*, *52*), while the rate constants for cleavage and product release are comparable for Mg^{2+} reactions (*22*, *30*, *52*).

Possibilities for the Catalytic Base. The localization of three distinct metal binding loci in the *Eco*RV active site, at and adjacent to the scissile phosphate, gives strong backing to the notion that the nucleophilic hydroxide ion is generated by ionization of an inner sphere water molecule with a lowered pK_a. This feature is common to most proposals for the *Eco*RV mechanism (*19*, *22*−*24*, *29*, *52*, *53*). However, there is no consensus about the identity of the catalytic base that accepts the proton from water. An early suggestion was that this role is played by the phosphate group located 3′-adjacent to the scissile phosphate (*51*); in a subsequent proposal, this idea was combined with the notion that only one metal ion per active site is required to facilitate chain scission (*54*). The suggestion that the 3′-phosphate functions as the catalytic base, however, now appears to be highly unlikely in view of its very low pK_a of approximately 1.5, together with the high pH optimum of the reaction at 8.5 (*29*). Further, strong evidence from both fluorescence and metal substitution experiments indicates that at least two metal ions per subunit are required for catalysis (*19*, *22*). The one-metal mechanism was rationalized by proposing

the existence of a distal Mg^{2+} binding site on a DNA phosphate at G*p*ATATC based on Mn^{2+} rescue of phosphorothioates (*55*); however, there is no crystallographic evidence for such a metal-binding locus, nor is there a suitable constellation of enzyme groups present to help form the site. Mn^{2+} is capable of rescuing low Mg^{2+}-dependent catalytic rates of mutants located throughout the protein structure (*26*, *56*), by virtue of its ability to function in the active site with weakened requirements for strict inner sphere ligand arrangements, and this explanation probably accounts for the Mn^{2+} rescue of the distal phosphorothioate substitution.

A second proposal is that the ionized forms of Glu45 and Asp36 together function as the catalytic base (*53*). This idea is based on pH−rate data suggesting that deprotonation of two acidic groups is required for DNA cleavage (a log-linear plot with a slope of 2 was observed). Moreover, the slope of this curve decreased to 1 in the weakly active D36E mutant enzyme. This proposal may be questioned on three separate grounds. First, there exist conflicting pH−rate data, which show a sharp bell-shaped profile with slopes of 1 on each limb, indicating instead that only one acidic group needs to be deprotonated during DNA cleavage by wild-type *Eco*RV (*29*). Second, while the catalytic efficiencies of single Asp36 mutants are decreased by 10^4−10^5-fold, combining a D36N mutant with the K38M substitution yielded a double-mutant *Eco*RV enzyme that retains 2% of wild-type activity (*26*). This strong reconstitution of activity makes it unlikely that D36 functions as the catalytic base. Third, structural data show that the side chain of Asp36 is not positioned sufficiently close to the scissile phosphate, even in the product complexes (Figure 2B). Together, these data suggest that a role for Asp36 as the catalytic base is unlikely, although ruling out such a role for Glu45 is less definitive and is based primarily on X-ray data showing that this side chain (when well-ordered) invariably ligates a metal ion directly in both substrate and product complexes. An alternative proposed role for Asp36 is that it functions together with Lys38 to modulate the electrostatic potential in the active site cleft (*26*).

The third proposal for the catalytic base is Lys92 (*23*, *25*, *29*), which is positioned appropriately with respect to the scissile phosphate in substrate complexes. Mutants at Lys92 are severely compromised in catalysis (*31*), but attempts to reconstitute K92A mutant activity with a series of exogenous ligands varying in basicity were unsuccessful (*26*). This proposal, therefore, relies primarily on X-ray structures showing the orientation of the side chain in substrate complexes. In the catalytic model proposed here, the reoriented scissile phosphate moves significantly away from Lys92, so the amine may no longer be appropriately positioned in the preattack conformation. However, after the phosphate−site III metal translocation (Figure 10), the Asp90 carboxylate may no longer ligate a metal ion [Asp90−M^{2+} ligation is absent in three of the four K38A subunits (Figure 8)]. As the metal ion moves together with the scissile phosphate, the pK_a of Asp90 will likely rise, making it also a reasonable candidate for accepting the proton in the catalytic step. The finding that the D90E mutant retains high catalytic activity, while D90A is nearly completely inactive, supports this proposal (*30*). In contrast, the central importance of Asp74 in ligating metal ions in all three sites, and probably also in facilitating the proposed metal translocation, is consistent with the inactivity of the D74E mutant (*30*).

Clearly, much attention has been focused on the identity of the catalytic base, but another possibility is that the DNA cleavage reaction is in fact capable of proceeding efficiently without such assistance. Simulations using a semiempirical PDLD method showed that deprotonation of water by either a phosphate or carboxylate group in *Bam*HI is considerably less favorable than metal-catalyzed deprotonation, with proton transfer to bulk solvent (*57*). The calculations did not address the favorability of lysine to provide general base assistance, but given the potential of a protonated Lys92 to promote DNA binding and bending, and the likelihood of a high pK_a in the vicinity of the DNA phosphates, the potential for this side chain to be present in the appropriate uncharged form may not be great.

Integration of Two-Metal and Three-Metal Models. The new catalytic model proposed here integrates features of previously proposed two- and three-metal models. In the three-metal catalytic model (*24*−*26*, *29*), DNA cleavage takes place without further significant rearrangement compared with what is observed in substrate complexes. Metals bind in each of sites I−III, where they presumably function to neutralize the incipient additional negative charge in the transition state (site III metal), to ionize a water molecule for protonation of the departing 3′-oxyanion (site III metal), and to deprotonate the attacking water molecule for generation of the hydroxide ion nucleophile (site I metal). The site I metal also ligates a second water that bridges to the 3′-adjacent phosphate, providing a structural rationale for the importance of this moiety as shown by phosphorothioate substitution experiments (*51*). The metal in site II is proposed to play a structural role.

By contrast, two-metal ion models have in common a rearrangement of the scissile phosphate prior to catalysis, bringing this moiety into appropriate juxtaposition with metal ions bound approximately in sites II and III (*19*, *22*, *23*, *27*, *30*, *53*). This is required since, in the substrate complex, sites II and III are oriented perpendicular to the apical direction of the trigonal bipyramidal transition state configuration, rather than parallel to it as required for the metals to perform their necessary functions. A weakness of these two-metal models is that they do not take into account the site I metal, now found to be occupied by Ca^{2+}, Mn^{2+}, or Mg^{2+} in six different uncleaved and cleaved ternary complex structures (refs *24* and *25* and Table 1; it should be noted, however, that in each of these structures either the DNA or the enzyme was modified). By contrast, the primary weakness of the three-metal model is the failure to simultaneously observe metals bound in sites I and III. While we have previously proposed that the co-occupancy of these sites is not observed in substrate complexes because of lattice forces that prevent cleavage in the *P*1 crystalline environment, another possibility is that the two sites actually are never simultaneously occupied, and that it is the local rearrangement of the phosphate group that is blocked in the *P*1 crystal form. In view of the K38A structures presented here, it now appears that the latter possibility is more compelling.

The new model integrates the proposed conformational change together with key functional roles for all three metal sites, and is based on the observation of very similar metal site positions and inner sphere ligations in the cleaved K38A

complexes, as observed in uncleaved complexes. These findings are made more robust by the observation that identical metal sites are found in the distinct monoclinic and primitive crystal forms (Table 1), which provides a measure of confidence against the possibility of artifacts arising from crystal packing forces. Because crystals of binary, uncleaved *Eco*RV−DNA complexes in the new monoclinic form have not been obtained, we do not know whether the enzyme is active in this lattice. Nonetheless, the new form is the only example of a metal-bound *Eco*RV ternary complex analyzed in a lattice other than the primitive triclinic one, which does not support enzyme activity (*23*, *32*).

While early two-metal models were formulated in fairly general terms (*19*, *22*, *23*), more recently the proposed conformational change of the scissile phosphate was analyzed with molecular dynamics simulations beginning from structures of the wild-type uncleaved ternary complex with metal ions bound in sites II and III (*27*, *30*). The simulations show that the phosphate undergoes a transition to a position 3.4 Å from its location in the substrate complex, and only 1.6 Å from the position of the 5′-phosphate in product complexes, similar to what is observed in the K38A structures (Figures 7B and 9). In the simulation, the rearrangement included a change in the sugar pucker of thymidine from C3′-endo to C2′-endo, while the metal ions changed coordination such that the nonesterified phosphate oxygens each ligated a distinct metal bound in site II and site III, respectively. Although the metal sites that are occupied differ, the simulations nonetheless support the notion that flipping of the scissile phosphate deeper into the active site prior to cleavage is energetically feasible (*30*). However, an important distinction is that, in the simulations, the assumption was made that two metal ions were bound before the rearrangement occurred, while the model we propose here invokes the conformational change after only one metal binds first in site III, consistent with the fluorescence data as described above (*22*).

A further simulation was also conducted which incorporated an assumption that Glu45 is the catalytic base; after the flipped phosphate conformation was obtained, −OH was attached to the phosphorus and a proton was attached to Glu45, and molecular dynamics was continued with the phosphorus assuming a trigonal bipyramid configuration (*27*). This simulation resulted in the movement of a metal ion to a position between the phosphate and the backbone of Gln69, as observed in the crystal structure of the product complex (Figure 8C). On the basis of these data, it was concluded that the transition state for phosphoryl transfer in *Eco*RV occurs within the active site in a position that strongly resembles the product complex. This is in contrast to the experimental findings here, which suggest instead that cleavage occurs with metal ions at sites I and II, rather than with metals located as in the product complex. Given the significant barrier to reaching the transition state, it appears to us to be more likely that cleavage occurs without requiring a further energetically costly rearrangement which might also involve reconfiguration of the center TA step to produce the cross-strand stacking of the adenines. Clearly, the structures indicate that at least for the weakly active K38A mutant, attaining the conformation seen in the wild-type product complex is not a requirement for phosphoryl transfer to occur. Of course, the differences may reflect an actual distinction in the structural pathway between wild-type *Eco*RV and K38A; another possibility is that catalysis might be possible in both configurations (or an array of different intermediate configurations) with a stochastic distribution among individual molecules.

In summary, the structures of K38A reported here represent the first experimental views of the scissile phosphate group at an intermediate location between the uncleaved and cleaved positions seen in wild-type *Eco*RV structures. Further, the two observed metal sites are very similar to those previously visualized in numerous examples of uncleaved *Eco*RV complexes, and they adopt nearly identical positions in the two structures determined here in distinct crystal lattice environments. Together, these observations provide a compelling rationale for our hypothesis that the pre-transition state configuration in *Eco*RV features a constellation of active site groups arranged in a manner highly similar to that observed in these structures of K38A.

Concluding Perspective. The extensive investigations into the *Eco*RV mechanism in many laboratories illustrate clearly the inherent difficulties involved in precisely correlating enzymological data with X-ray crystal structures, even when the structures are at very high resolutions and the kinetics are performed with exacting rigor. Another well-known example illustrating this theme is the hammerhead ribozyme, for which a similarly exhaustive set of enzymology and crystallography experiments still fails to produce a clear consensus for the structurally based stereochemical pathway of strand scission (*58*, *59*). These systems stand in sharp contrast to enzymes such as *Bam*HI and *Bgl*I endonucleases, in which the initial ternary enzyme−DNA−metal ion structures immediately suggested a well-defined metal-dependent phosphoryl transfer mechanism (*60*, *61*). Clearly, the distinction lies in whether the initially formed enzyme−substrate complexes trapped in crystals are close to the preattack conformation or whether additional, energetically costly rearrangements are required. A potential hazard is that restriction enzymes such as *Bam*HI and *Bgl*I may remain understudied, and our understanding of them based on heavy reliance on X-ray data may include misinterpretations, because, given the appearance of a "solved" mechanism, the rigorous kinetic data with which to make important correlations are never obtained.

ACKNOWLEDGMENT

Portions of this research were carried out at the Stanford Synchrotron Radiation Laboratory (Palo Alto, CA), a national user facility operated by Stanford University on behalf of the U.S. Department of Energy, Office of Basic Energy Sciences. The SSRL Structural Molecular Biology Program is supported by the Department of Energy, Office of Biological and Environmental Research, and by the National Institutes of Health, National Center for Research Resources, Biomedical Technology Program, and the National Institute of General Medical Sciences.

REFERENCES

1. Horton, N. C., and Perona, J. J. (2001) Making the most of metal ions, *Nat. Struct. Biol. 8*, 290−293.
2. West, K. L., Meczes, E. L., Thorn, R., Turnbull, R. M., Marshall, R., and Austin, C. A. (2000) Mutagenesis of E477 or K505 in the B′ domain of human topoisomerase II β increases the

requirement for magnesium ions during strand passage, *Biochemistry 39*, 1223−1233.
3. Hickman, A. B., Li, Y., Mathew, S. V., May, E. W., Craig, N. L., and Dyda, F. (2000) Unexpected structural diversity in DNA recombination: the restriction endonuclease connection, *Mol. Cell 5*, 1025−1034.
4. de Laat, W. L., Appeldoorn, E., Jaspers, N. G., and Hoeijmakers, J. H. (1998) DNA structural elements required for ERCC1-XPF endonuclease activity, *J. Biol. Chem. 273*, 7835−7842.
5. Ban, C., and Yang, W. (2000) Structural basis for MutH activation in *E. coli* mismatch repair and relationship of MutH to restriction endonucleases, *EMBO J. 17*, 1526−1534.
6. Kovall, R. A., and Matthews, B. W. (1998) Structural, functional, and evolutionary relationships between λ-exonuclease and the type II restriction endonucleases, *Proc. Natl. Acad. Sci. U.S.A. 95*, 7893−7897.
7. Tsutakawa, S. E., Muto, T., Kawate, T., Jingami, H., Kunishima, N., Ariyoshi, M., Kohda, D., Nakagawa, M., and Morikawa, K. (1999) Crystallographic and functional studies of very short patch repair endonuclease, *Mol. Cell 3*, 621−628.
8. Pingoud, A., and Jeltsch, A. (2001) Structure and function of type II restriction endonucleases, *Nucleic Acids Res. 29*, 3705−3727.
9. Beese, L. S., and Steitz, T. A. (1991) Structural basis for the 3′-5′ exonuclease activity of *Escherichia coli* DNA polymerase I: a two metal ion mechanism, *EMBO J. 10*, 25−33.
10. Yang, W., and Steitz, T. A. (1995) Recombining the structures of HIV integrase, RuvC and RNase H, *Structure 3*, 131−134.
11. Perona, J. J. (2002) Type II restriction endonucleases, *Methods 28*, 353−364.
12. Schildkraut, I., Banner, C. D. B., Rhodes, C. S., and Parekh, S. (1984) The cleavage site for the restriction endonuclease EcoRV is 5′-GAT/ATC-3′, *Gene 27*, 327−329.
13. Taylor, J. D., and Halford, S. E. (1989) Discrimination between DNA sequences by the EcoRV restriction endonuclease, *Biochemistry 28*, 6198−6207.
14. Martin, A. M., Horton, N. C., Lusetti, S., Reich, N. O., and Perona, J. J. (1999) Divalent metal dependence of site-specific DNA binding by EcoRV endonuclease, *Biochemistry 38*, 8430−8439.
15. Martin, A. M., Sam, M. D., Reich, N. O., and Perona, J. J. (1999) Structural and energetic origins of indirect readout in site-specific DNA cleavage by a restriction endonuclease, *Nat. Struct. Biol. 6*, 269−277.
16. Engler, L. E., Welch, K. K., and Jen-Jacobson, L. (1997) Specific binding by EcoRV endonuclease to its DNA recognition site GATATC, *J. Mol. Biol. 269*, 82−101.
17. Reid, S. L., Parry, D., Liu, H. H., and Connolly, B. A. (2001) Binding and recognition of GATATC target sequences by the EcoRV restriction endonuclease: a study using fluorescent oligonucleotides and fluorescence polarization, *Biochemistry 40*, 2484−2494.
18. Taylor, J. D., Badcoe, I. G., Clarke, A. R., and Halford, S. E. (1991) EcoRV restriction endonuclease binds all DNA sequences with equal affinity, *Biochemistry 30*, 8743−8753.
19. Vipond, I. B., Baldwin, G. S., and Halford, S. E. (1995) Divalent metal ions at the active sites of the EcoRV and EcoRI restriction endonucleases, *Biochemistry 34*, 697−704.
20. Vipond, I. B., and Halford, S. E. (1995) Specific DNA recognition by EcoRV restriction endonuclease induced by calcium ions, *Biochemistry 34*, 1113−1119.
21. Perona, J. J., and Martin, A. M. (1997) Conformational transitions and structural deformability of EcoRV endonuclease revealed by crystallographic analysis, *J. Mol. Biol. 273*, 207−225.
22. Baldwin, G. S., Vipond, I. B., and Halford, S. E. (1995) Rapid reaction analysis of the catalytic cycle of the EcoRV restriction endonuclease, *Biochemistry 34*, 705−714.
23. Kostrewa, D., and Winkler, F. K. (1995) Mg^{2+} binding to the active site of EcoRV endonuclease: a crystallographic study of complexes with substrate and product DNA at 2 Å resolution, *Biochemistry 34*, 683−696.
24. Horton, N. C., Newberry, K. J., and Perona, J. J. (1998) Metal ion-mediated substrate-assisted catalysis in type II restriction endonucleases, *Proc. Natl. Acad. Sci. U.S.A. 95*, 13489−13494.
25. Horton, N. C., Connolly, B. A., and Perona, J. J. (2000) Inhibition of *Eco*RV endonuclease by deoxyribo-3′-S-phosphorothiolates: A high-resolution X-ray-crystallographic study, *J. Am. Chem. Soc. 122*, 3314−3324.
26. Horton, N. C., Otey, C., Lusetti, S., Sam, M. D., Kohn, J., Martin, A. M., Ananthnarayan, V., and Perona, J. J. (2002) Electrostatic contributions to site specific DNA cleavage by EcoRV endonuclease, *Biochemistry 41*, 10754−10763.
27. Thomas, M. P., Brady, R. L., Halford, S. E., Sessions, R. B., and Baldwin, G. S. (1999) Structural analysis of a mutational hotspot in the EcoRV restriction endonuclease: a catalytic role for a main chain carbonyl group, *Nucleic Acids Res. 27*, 3438−3445.
28. Sam, M. D., Horton, N. C., Nissan, T. A., and Perona, J. J. (2001) Catalytic efficiency and sequence selectivity of a restriction endonuclease modulated by a distal manganese ion binding site, *J. Mol. Biol. 306*, 851−861.
29. Sam, M. D., and Perona, J. J. (1999) Catalytic roles of divalent metal ions in phosphoryl transfer by EcoRV endonuclease, *Biochemistry 38*, 6576−6586.
30. Baldwin, G. S., Sessions, R. B., Erskine, S. G., and Halford, S. E. (1999) DNA cleavage by the EcoRV restriction endonuclease: roles of divalent metal ions in specificity and catalysis, *J. Mol. Biol. 288*, 87−103.
31. Selent, U., Reuter, T., Koehler, E., Liedtke, M., Thielking, V., Alves, J., Oelgeschleager, T., Wolfes, H., Peters, F., and Pingoud, A. (1992) A site-directed mutagenesis study to identify amino acid residues involved in the catalytic function of the restriction endonuclease EcoRV, *Biochemistry 31*, 4808−4815.
32. Horton, N. C., and Perona, J. J. (2000) Crystallographic snapshots along a protein-induced DNA-bending pathway, *Proc. Natl. Acad. Sci. U.S.A. 97*, 5729−5734.
33. Winkler, F. K., Banner, D. W., Oefner, C., Tsernoglou, D., Brown, R. S., Heathman, S. P., Bryan, R. K., Martin, P. D., Petratos, K., and Wilson, K. S. (1993) The crystal structure of EcoRV endonuclease and of its complexes with cognate and non-cognate DNA fragments, *EMBO J. 12*, 1781−1795.
34. Ho, S. N., Hunt, H. D., Horton, R. M., Pullen, J. K., and Pease, L. R. (1989) Site-directed mutagenesis by overlap extension using the polymerase chain reaction, *Gene 77*, 51−59.
35. Pope, B., and Kent, H. M. (1996) High efficiency 5 min transformation of *Escherichia coli*, *Nucleic Acids Res. 24*, 536−537.
36. Vipond, I. B., and Halford, S. E. (1996) Random mutagenesis targeted to the active site of the EcoRV restriction endonuclease, *Biochemistry 35*, 1701−1711.
37. Vermote, C. L., Vipond, I. B., and Halford, S. E. (1992) EcoRV restriction endonuclease: communication between DNA recognition and catalysis, *Biochemistry 31*, 6089−6097.
38. Leslie, A. G. (1999) Integration of macromolecular diffraction data, *Acta Crystallogr. D55*, 1696−1702.
39. Evans, P. R. (1993) *Proceedings of CCP4 Study Weekend*, pp 114−122, Daresbury Laboratory, Warrington, U.K.
40. Brunger, A. T., Kuriyan, J., and Karplus, M. (1987) Crystallographic R-factor refinement by molecular dynamics, *Science 235*, 458−460.
41. Brünger, A. T., Adams, P. D., Clore, G. M., DeLano, W. L., Gros, P., Grosse-Kunstleve, R. W., Jiang, J. S., Kuszewski, J., Nilges, M., Pannu, N. S., Read, R. J., Rice, L. M., Simonson, T., and Warren, G. L. (1998) Crystallography & NMR system: A new software suite for macromolecular structure determination, *Acta Crystallogr. D54*, 905−921.
42. Sack, J. S. (1988) CHAIN: A crystallographic modelling program, *J. Mol. Graphics 6*, 224−225.
43. McRee, D. E. (1999) XtalView/Xfit: A versatile program for manipulating atomic coordinates and electron density, *J. Struct. Biol. 125*, 156−165.
44. Stahl, F., Wende, W., Wenz, C., Jeltsch, A., and Pingoud, A. (1998) Intra- vs intersubunit communication in the homodimeric restriction enzyme EcoRV: Thr37 and Lys38 involved in indirect readout are only important for the catalytic activity of their own subunit, *Biochemistry 37*, 5682−5688.
45. Glusker, J. P. (1991) Structural aspects of metal liganding to functional groups in proteins, *Adv. Protein Chem. 42*, 1−76.
46. Williams, L. D., and Maher, L. J., III (2000) Electrostatic mechanisms of DNA deformation, *Annu. Rev. Biophys. Biomol. Struct. 29*, 497−521.
47. Lagunavicius, A., and Siksnys, V. (1997) Site-directed mutagenesis of putative active site residues of MunI restriction endonuclease: replacement of catalytically essential carboxylate residues triggers DNA binding specificity, *Biochemistry 36*, 11086−11092.
48. Lagunavicius, A., Grazulis, S., Balciunaite, E., Vainius, D., and Siksnys, V. (1997) DNA binding specificity of MunI restriction endonuclease is controlled by pH and calcium ions: involvement of active site carboxylate residues, *Biochemistry 36*, 11093−11099.

49. Newman, M., Strzelecka, T., Dorner, L. F., Schildkraut, I., and Aggarwal, A. K. (1995) Structure of BamHI endonuclease bound to DNA: Partial folding and unfolding on DNA bending, *Science 269*, 656−663.
50. Hiller, D. A., Fogg, J. M., Martin, A. M., Beechem, J. M., Reich, N. O., and Perona, J. J. (2003) Simultaneous DNA binding and bending by EcoRV endonuclease observed by real-time fluorescence, *Biochemistry 42*, 14375−14385.
51. Jeltsch, A., Alves, J., Wolfes, H., Maass, G., and Pingoud, A. (1993) Substrate-assisted catalysis in the cleavage of DNA by the EcoRI and EcoRV restriction enzymes, *Proc. Natl. Acad. Sci. U.S.A. 90*, 8499−8503.
52. Sam, M. D., and Perona, J. J. (1999) Mn^{2+}-dependent catalysis by restriction enzymes: Pre-steady-state analysis of *Eco*RV endonuclease reveals burst kinetics and the origins of reduced activity, *J. Am. Chem. Soc. 121*, 1444−1447.
53. Stanford, N. P., Halford, S. E., and Baldwin, G. S. (1999) DNA cleavage by the EcoRV restriction endonuclease: pH dependence and proton transfers in catalysis, *J. Mol. Biol. 288*, 105−116.
54. Groll, D. H., Jeltsch, A., Selent, U., and Pingoud, A. (1997) Does the restriction endonuclease EcoRV employ a two-metal-ion mechanism for DNA cleavage, *Biochemistry 36*, 11389−11401.
55. Jeltsch, A., Maschke, H., Selent, U., Wenz, C., Kohler, E., Connolly, B. A., Thorogood, H., and Pingoud, A. (1995) DNA binding specificity of the EcoRV restriction endonuclease is increased by Mg^{2+} binding to a metal ion binding site distinct from the catalytic center of the enzyme, *Biochemistry 34*, 6239−6246.
56. Vipond, I. B., Moon, B.-J., and Halford, S. E. (1996) An isoleucine to leucine mutation that switches the cofactor requirement of the EcoRV restriction endonuclease from magnesium to manganese, *Biochemistry 35*, 1712−1721.
57. Fuxreiter, M., and Osman, R. (2001) Probing the general base catalysis in the first step of BamHI action by computer simulations, *Biochemistry 40*, 15017−15023.
58. Dunham, C. M., Murray, J. B., and Scott, W. G. (2003) A helical twist-induced conformational switch activates cleavage in the hammerhead ribozyme, *J. Mol. Biol. 332*, 327−336.
59. Stage-Zimmerman, T. K., and Uhlenbeck, O. C. (1998) Hammerhead ribozyme kinetics, *RNA 4*, 875−889.
60. Viadiu, H., and Aggarwal, A. K. (1998) The role of metals in catalysis by the restriction endonuclease BamHI, *Nat. Struct. Biol. 5*, 910−916.
61. Newman, M., Lunnen, K., Wilson, G., Greci, J., Schildkraut, I., and Phillips, S. E. V. (1998) Crystal structure of restriction endonuclease BglI bound to its interrupted DNA recognition sequence, *EMBO J. 17*, 5466−5476.

BI0499056